Small Methods

small
methods
www.small-methods.com

RESEARCH ARTICLE

Photoresponsive Liquid Grippers for Multi-Dimensional Droplet Manipulation

Yu Pu | Lixin Jiang | Xin Qing | Yitian Ming | Jiaqiang Li | Lang Qin | Yanlei Yu

College of Smart Materials and Future Energy, State Key Laboratory of Molecular Engineering of Polymers, Fudan University, Shanghai, P. R. China

Correspondence: Lang Qin (qinlang@fudan.edu.cn) | Yanlei Yu (ylyu@fudan.edu.cn)

Received: 30 October 2025 | **Revised:** 11 February 2026 | **Accepted:** 25 February 2026

Keywords: droplet manipulation | liquid crystal polymers | liquid grippers | photodeformation | wettability

ABSTRACT

Droplet manipulation has significant value in a wide range of areas, such as microfluidics, medical diagnosis, and detection. However, high-precision droplet manipulation with arbitrary control on an open surface still poses a substantial challenge, particularly in 3D droplet manipulation. Here, we propose a bilayer photoresponsive liquid gripper (PLG), which integrates an "adhesive layer" and an "actuation layer" to enable sustainable capture and release for precise 3D droplet manipulation of high-viscosity fluids (e.g., blood, serum, and pH solutions). The "adhesive layer" featuring a superhydrophobic microarrayed polydimethylsiloxane surface allows nondestructive droplet capture. Meanwhile, the "actuation layer" leverages the photo-induced bending of photodeformable crosslinked liquid crystal polymers to release the droplet without altering its surface wettability. Moreover, by simply adjusting the microstructures of its surface, PLG allows the selective capture of droplets of particular sizes, providing a new tool for droplet screening. Biochemical reactions, including blood detection, neutralization reactions, and immunoassays, are successfully demonstrated via the PLG system, underscoring its utility as an effective and versatile platform for complex droplet manipulation, biological analysis, and routine biochemical investigations.

1 | Introduction

Discrete droplets serve as versatile microreactors and carriers in diverse applications ranging from biochemical assays [1–4] and biomedical diagnostics [5, 6] to cell culture [7, 8] and oil/water separation [9, 10]. The precise control of droplet dynamics on surfaces is critical for advancing these technologies. Conventional 2D manipulation techniques, limited to in-plane operations such as transportation, fusion, and separation, face challenges in meeting the growing demands of trace analyte detection and advanced material synthesis [11, 12]. Thus, developing 3D droplet manipulation strategies is essential to maximize their utility in diverse applications. The advantages of 3D manipulation include the ability to perform precise out-of-plane operations, such as vertical transfer and interactions between noncoplanar points, which are essential for constructing complex 3D fluidic architectures [13–16]. Moreover, this approach increases processing speed and reduces cross-contamination risks in lab-on-a-chip systems [17]. It also provides greater operational flexibility, functionality, and volumetric capacity compared to conventional 2D platforms [18–20]. Inspired by solid-object grippers utilizing capture-and-release mechanisms, liquid grippers have emerged to overcome gravitational constraints and droplet-substrate adhesion through vertical force application, thereby achieving precise 3D droplet manipulation [13–15]. These systems surpass conventional responsive surfaces by offering accelerated operational speeds and minimized contamination risks.

The process of 3D droplet manipulation by a liquid gripper involves three steps: droplet capture, transfer, and release. The capture of droplets can be facilitated by introducing high adhesion on the gripper surface. However, excessively high adhesion forces often result in difficulty in droplet release from the gripper surface, thereby constraining the flexibility of droplet manipulation across different surfaces. Thus, the reversible switch of the adhesion force and wettability of the surface under external stimuli such as magnetic fields [21–23], electricity [24], and light [25–27] offers an effective method for liquid transportation. For example, Yan et al. reported a laser-based pick-and-place droplet gripper that rapidly transforms surface properties from hydrophobic to hydrophilic by generating uniform charges through a photothermal-induced pyroelectric effect, thereby enabling controllable droplet release [28]. However, dielectric breakdown and charge screening effects readily occur in air and conductive media, thereby limiting the practical applicability [29, 30]. Sun et al. demonstrated a novel programmable wettability arrays that switch the surface droplet adhesion status via the photothermal-induced shrinkage of graphene oxide-hybridized hydrogel under NIR irradiation [31]. Nevertheless, the reliance on photothermal energy transformation entails an unavoidable temperature elevation that precludes the nondestructive transport of thermal-sensitive enzymes and proteins. Moreover, the wetting interaction between droplets and the surface renders the nondestructive and non-polluting transportation of trace amounts of liquid unfeasible, thereby restricting its application in trace liquid analysis [32–34].

In contrast to static interfaces, stimuli-responsive topographic surfaces exhibit dynamic reconfiguration capabilities through reversible morphological transitions under external triggers, establishing a promising platform for multi-dimensional droplet control [35]. Representative systems employing superhydrophobic microstructured surfaces composed of pillars or walls demonstrate bending behaviors that generate geometric asymmetry. Such structural transitions establish gradient capillary forces through spatially modulated surface tension distributions, thereby enabling directional droplet propulsion [18, 19]. This fundamental mechanism can be strategically adapted in liquid gripper designs to achieve nondestructive manipulation of microdroplets with precision. Notably, the integration of light-driven methods with such grippers introduces transformative advantages, including contactless operation, spatiotemporally resolved control, and enhanced biological compatibility, which are critical attributes for advancing analytical applications in biosensing and diagnostic technologies [36–38]. Liquid crystal polymers (LCPs) have emerged as particularly suitable photodeformable substrates for such applications, leveraging their unique capacity for reversible macroscopic shape morphing [39]. This photomechanical response originates from photo-isomerization-induced mesogen reorientation within their hierarchically ordered architecture, enabling programmable actuation with spatiotemporal precision under isothermal conditions [40–44]. Through rational material engineering, LCP-based systems present versatile platforms for developing light-powered microfluidic manipulators with operational versatility.

Herein, we propose a facile strategy to construct a bilayer PLG and the corresponding operating platform to achieve precise and rapid multi-directional 3D droplet manipulation (Figure 1a). The bilayer PLG comprises a microarrayed polydimethylsiloxane (PDMS) layer and a photodeformable crosslinked liquid crystal polymer (CLCP) layer. PDMS was selected as the adhesive layer not only for its intrinsic hydrophobicity, excellent machinability, and mechanical compliance, which facilitate the fabrication of superhydrophobic micro/nanostructures for nondestructive droplet capture, but also for its superior interfacial compatibility with CLCP, enabling robust integration without additional adhesives. Meanwhile, CLCP serves as the photoactive actuation layer due to its remarkable photomechanical properties, undergoing substantial and reversible macroscopic deformation under specific wavelength light irradiation. This efficient transduction of light into mechanical force enables controlled droplet release through photo-induced bending of the CLCP layer (Figure 1b). Owing to the reversible photodeformation of the CLCP layer, a sustainable capture-and-release process has been achieved for various liquids, even high-viscosity biological samples such as blood. Moreover, by simply adjusting the microstructures of its surface, PLG allows the selective capture of droplets of particular sizes, providing a new tool for droplet screening. Ultimately, we demonstrate biochemical reactions, including blood detection, neutralization reactions, and immunoassays, through 3D droplet manipulation of the PLG. This demonstrates its potential as a versatile, programmable, and sustainable strategy for droplet manipulation, with broad biomedical applications extending from droplet sorting to biological diagnostics.

2 | Results and Discussion

To construct a PLG and achieve 3D droplet manipulation, at least two crucial requirements need to be fulfilled: (1) the gripper's topographic interface must generate adhesion forces that exceed both gravitational effects on the droplet and substrate–droplet adhesion forces to ensure stable capture; (2) the PLG architecture must enable rapid, large-magnitude deformation to dynamically modulate the interfacial stress states of the droplet, thereby overcoming gripper–droplet adhesion to achieve controlled release. Thus, a surface combining superhydrophobicity with high adhesion is critically important for low-loss liquid capture and transport when utilized in PLG. To meet the demands of droplet retention while ensuring favorable biocompatibility, we fabricated a PDMS layer with a rose petal-like microstructure, incorporating an array of micropillars (Figure 1c). This surface exhibits a contact angle (CA) of approximately 150° and demonstrates an adhesion force of ∼88 μN, which is sufficient to counteract gravity and stably suspend a 9.0 μL water droplet. Droplet release fundamentally involves a transition from static equilibrium to dynamic motion. To achieve droplet detachment from the PDMS surface, the initial mechanical equilibrium of the droplet must be disrupted. Because the adhesive force exerted by the PLG substrate is strictly normal to the surface plane, the PLG topography can be precisely modulated via the actuation layer. A robust photodeformable CLCP was employed as the actuation layer owing to its exceptional photodeformablity. The CLCP was synthesized via the copolymerization of an azobenzene-containing diacrylate monomer and a non-photoresponsive diacrylate monomer within the liquid crystal cell, resulting in a densely crosslinked nematic CLCP film (Figure 1d) [45]. Upon UV irradiation, the CLCP film exhibited significant photo-induced deformation, resulting in substantial bending of the PLG actuator (Figure 1e). The PLG system combines a superhydrophobic microarrayed PDMS layer for capturing droplets with low adhesion and a CLCP film that acts as a light-driven actuator. This integrated design enables reversible and size-selective droplet manipulation by reducing

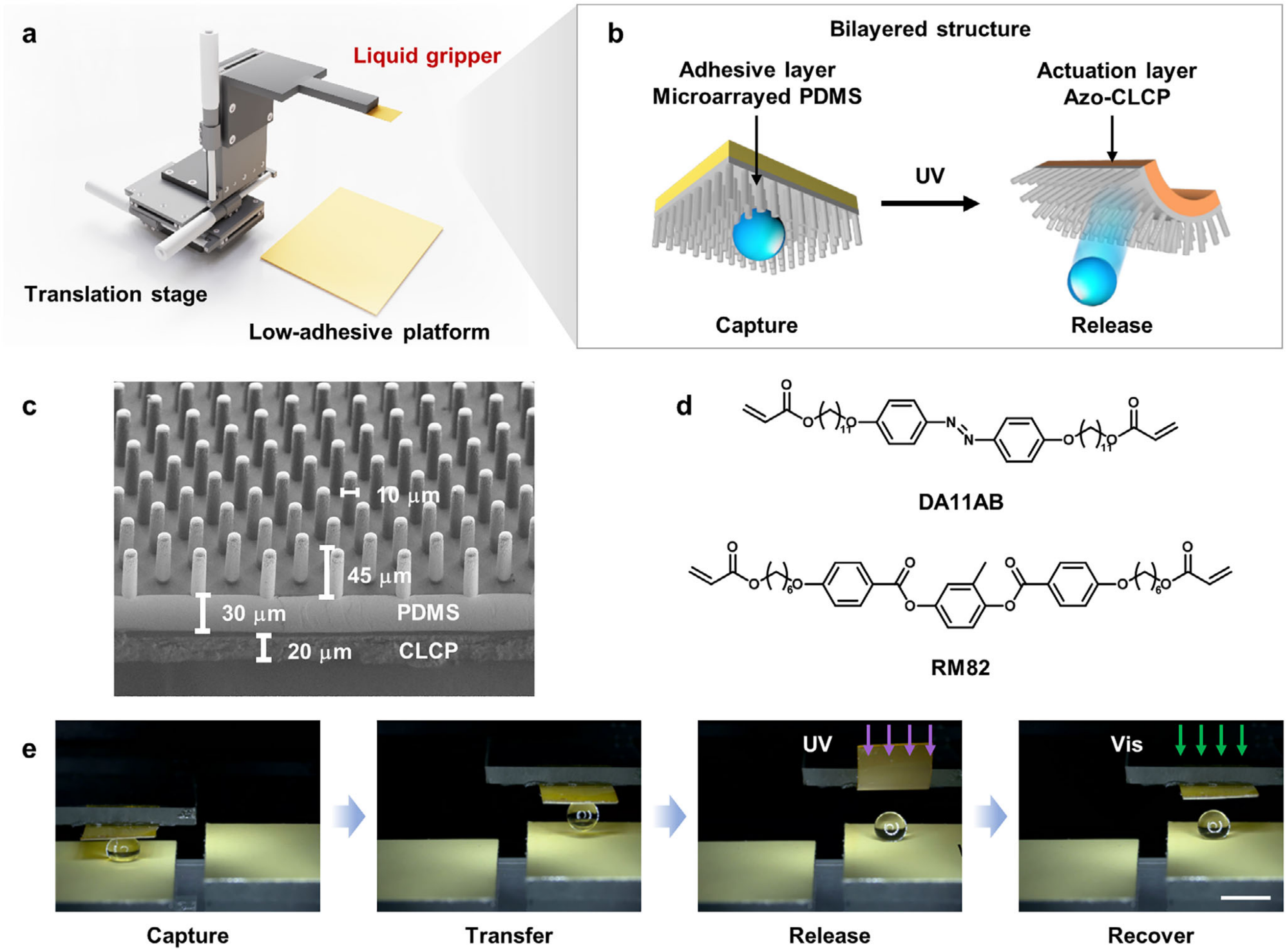

FIGURE 1 | (a) Schematic of the droplet manipulation equipment consisting of the photoresponsive liquid gripper (PLG) on the three-axis translation stage and the low-adhesive substrate. (b) Schematic illustration showing the bilayered structure of the PLG composed of an adhesive layer and an actuation layer. The adhesion layer is composed of microarrayed PDMS for the capture of droplets, and the actuation layer is composed of an azobenzene-containing crosslinked liquid crystal polymer (CLCP) film for the controllable release of droplets. (c) FESEM image of the microarrayed PDMS/CLCP bilayer. (d) Chemical structures of the monomers used for fabricating the CLCP film. (e) Water drop transportation between surfaces of different heights. The volume of the water drop is 3.0 µL. The scale bar is 2 mm.

adhesion hysteresis and transducing photomechanical energy into droplet ejection. The controlled shape change disrupts the droplet equilibrium, triggering a transition from pinning to sliding and enabling active, nondestructive release.

The light-controlled 3D droplet manipulation capability of the PLG was demonstrated by integrating the device onto a three-axis translational stage (Figure 1e). Owing to the sufficient adhesion provided by the microarrayed PDMS layer, the PLG effectively lifted droplets from low-adhesion substrates upon contact and securely immobilized them on the PDMS surface without residual contamination or droplet fragmentation. Following droplet transfer to the target location via the translational stage, localized UV irradiation (365 nm, 30 mW cm^{-2}) was applied to the upper layer of the CLCP, inducing rapid macroscopic deformation of the PLG and destabilizing the equilibrium of the suspended droplets within seconds (Video S1). Infrared thermography verified that under UV irradiation, the temperature of the PLG did not exceed the biologically safe threshold of 37°C (Figure S1). During this phase, the interplay between gravitational and adhesive forces prompts droplet sliding along an arcuate trajectory, converting gravitational potential energy into kinetic energy and accelerating droplet motion (Video S2). This energy-efficient mechanism minimizes the reliance on external pumps or mechanical components, significantly simplifying the device architecture. When the resultant force failed to sustain adequate centripetal force, the droplet detached from the PLG surface, enabling cross-interface liquid transport. Furthermore, the reversible photodeformation of the CLCP allowed the PLG to revert to its original conformation under visible light exposure (530 nm, 30 mW cm^{-2}), facilitating device reusability. This reusability, combined with wavelength-selective control, positions PLG as a sustainable and cost-effective solution for programmable liquid manipulation in lab-on-a-chip systems, organ-on-chip platforms, and adaptive soft robotics.

Droplet capture involves two critical processes: (1) effective adhesion between the PLG and droplets and (2) unhindered droplet detachment from the substrate surface. The realization of these two processes necessitates independent modulation of the surface properties. Through precise control of the

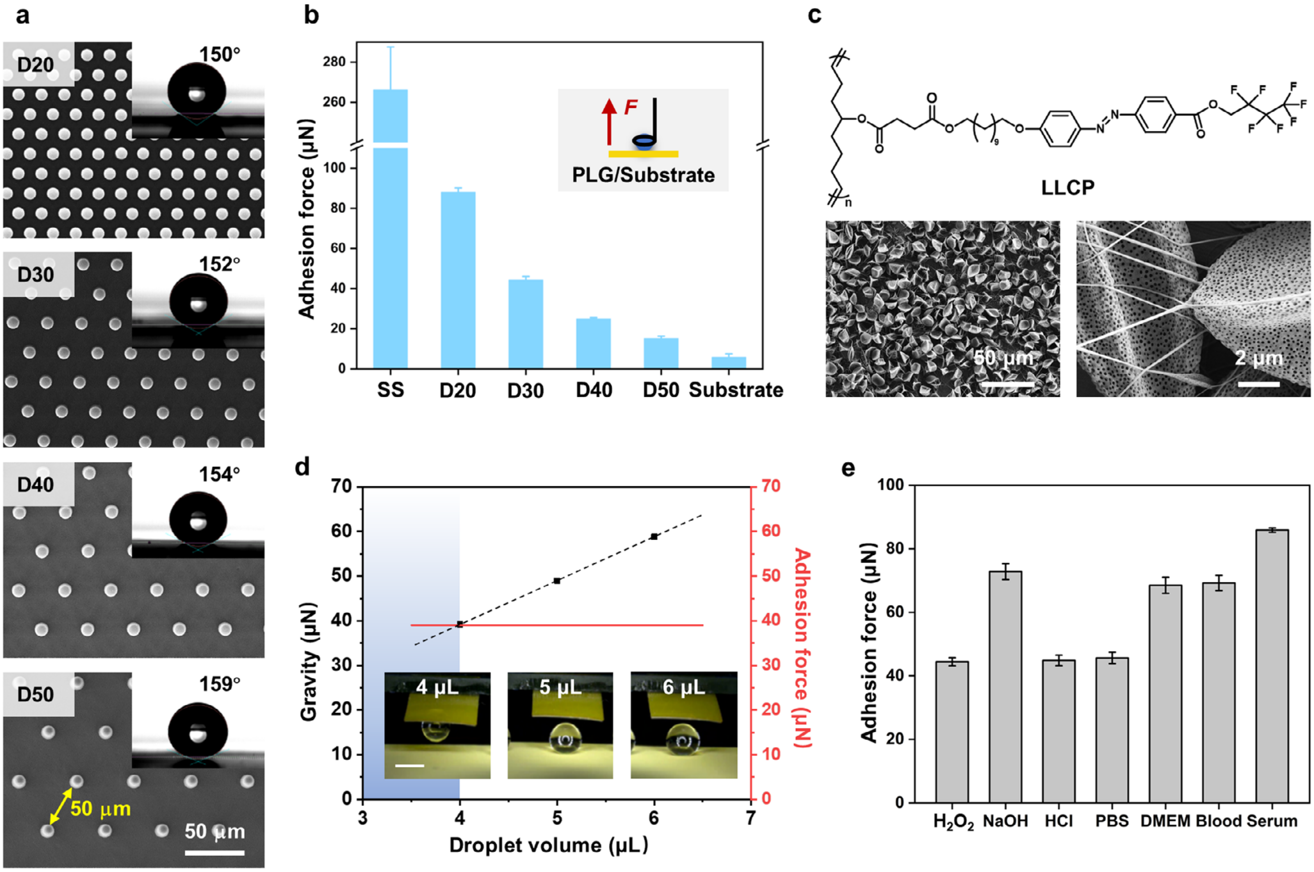

FIGURE 2 | (a) FESEM images showing the top view of microarrayed PDMS films with pillar center spacings of 20–50 μm (D20–D50). The inserted photographs show the contact angles (CAs) of a 3.0 μL water droplet on the surfaces of D20–D50. (b) Adhesive forces of water droplets on pure PDMS films, D20, D30, D40, D50, and low-adhesive substrate with different curvatures. (c) Chemical structure of the linear liquid crystal polymer and field-emission scanning electron microscopy (FESEM) images of the substrate fabricated by electrospinning. (d) Plot showing the magnitude of the droplet gravity force and the adhesive force difference between the PDMS and the substrate. The inserted photographs show the process of grabbing water droplets of sizes 6.0, 5.0, and 4.0 μL through D30. The scale bar is 1 mm. (e) Adhesive force of H_2O_2 (1 mol L^{-1}), NaOH (1 mol L^{-1}), HCl (1 mol L^{-1}), PBS buffer (1X), cell culture medium (Dulbecco's modified Eagle medium, DMEM), blood and serum on D30 (the microarrayed PDMS/CLCP bilayer with a center pillar spacing of 30 μm). The values of adhesion force are presented as mean ± standard deviation (SD) from three independent measurements ($n = 3$).

microarrayed PDMS pillar spacing, we effectively tuned the adhesive properties of the PLG, enabling both stable capture and volume-selective droplet screening. The microcolumn array architecture profoundly influences surface adhesion characteristics, primarily through interfacial cavity size variations [46]. Accordingly, we fabricated four PDMS microarray samples with pillar center-to-center spacings ranging from 20 to 50 μm (designated D20–D50) for performance evaluation (Figure 2a). Notably, all surface maintained contact angles (CAs) exceeding 150° regardless of pillar spacing, whereas their adhesive forces decreased systematically from 88 to 20 μN with increasing interpillar distance (Figure 2b). This observed reduction in adhesion can be attributed to the transition in the wetting state [20]. The superhydrophobic behavior of the microarrayed surface was determined to follow the Cassie model, in which air remains trapped beneath the droplet, resulting in low adhesion [47]. This was confirmed by depositing an ink-laden droplet onto the surface (Figure S2), and the absence of penetration into the microstructures demonstrates the presence of a composite solid–air interface characteristic of the Cassie wetting state.

Moreover, to ensure easy detachment of the droplets from the substrate, the substrate holding the droplets should maintain a lower adhesion than the microarrayed PDMS bottom layer of PLG [9, 48]. For efficient droplet detachment, we incorporated an electrospun mat substrate fabricated from a fluorinated alkyl-group-modified linear LCP (Figure 2c), which exhibited minimal adhesion (6 μN) while maintaining robust superhydrophobicity. Field-emission scanning electron microscopy (FESEM) characterization revealed a nanofibrous architecture featuring numerous spindle-like protrusions [49], which enhance surface roughness and thereby promote superhydrophobicity.

We fabricated a series of PLGs (PLG-D20 to PLG-D50) with tunable adhesion properties by integrating PDMS surfaces containing microarrays of varying spacing (20–50 μm). The droplet capture efficiency was found to obey the mechanical equilibrium condition: $G \leq F_{PLG} - F_{substrate}$, where G represents droplet gravity, and F_{PLG} and $F_{substrate}$ denote the adhesion forces of the PLG and substrate, respectively. For 2.0 μL droplets, the capture stability increased with decreasing array spacing, with PLG-D20 through PLG-D40 demonstrating reliable capture, whereas

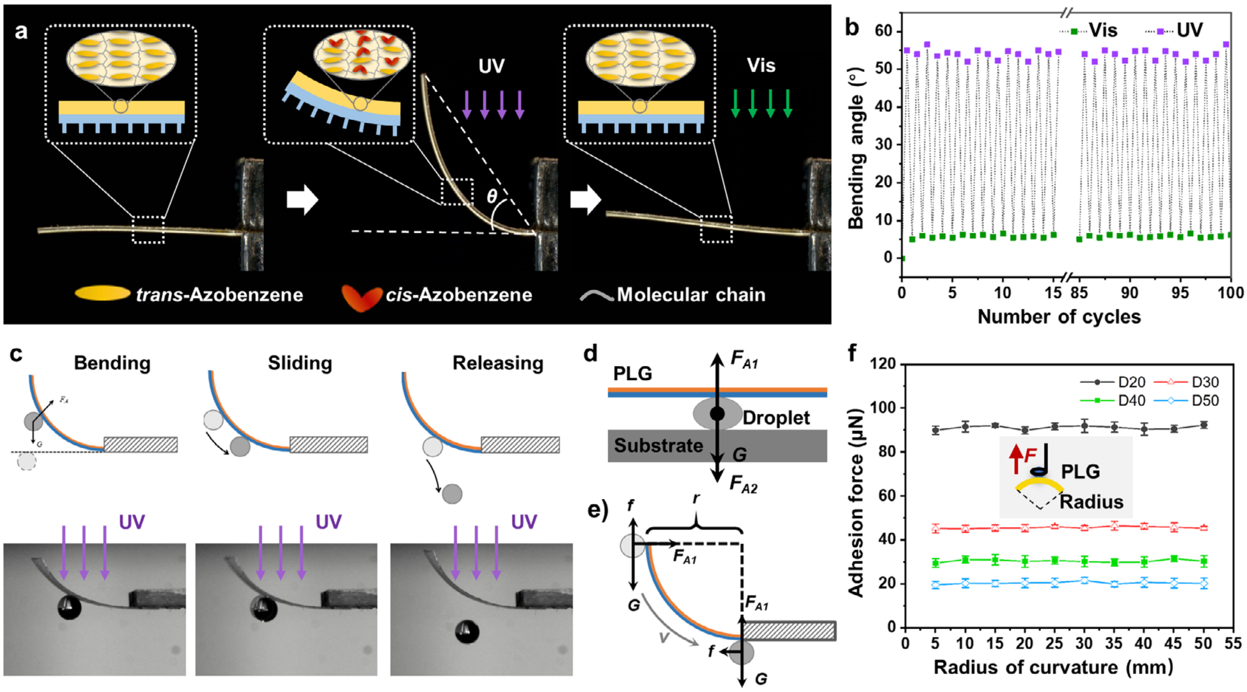

FIGURE 3 | (a) Photographs showing the bending and unbending behaviors of the PLG (10 mm × 10 mm) under irradiation with UV light (365 nm, 20 mW cm^{-2}) and visible light (530 nm, 30 mW cm^{-2}), respectively. The inserted illustrations show the photoresponsive deformation mechanism of the CLCP film induced by the reversible trans-cis isomerization of azobenzene. (b) Evaluation of the reversibility of the bilayer PLG in response to alternating irradiation with UV light (365 nm, 20 mW cm^{-2}, 10 s) and visible light (530 nm, 30 mW cm^{-2}, 10 s) for 100 cycles. (c) Schematic illustration and photographs of the photodeformation of the PLG and the water droplet release process. (d) Schematic diagram of the force of a droplet during the capture process. (e) Schematic diagram of the force of a droplet in the highest position (dotted pattern) and lowest position (solid pattern) that a water drop would pass through during the release process. (f) Adhesive forces of water droplets on D20, D30, D40, and D50 with different curvatures. The values of adhesion force are presented as mean ± SD from three independent measurements ($n = 3$).

PLG-D50 failed because of its lower adhesion force. Each PLG variant exhibited a characteristic maximum capture volume (e.g., 4.0 μL for PLG-D30, corresponding to the point where the droplet weight (39.2 μN) balanced the net adhesion force) (Figure 2d, Video S3). This quantitative relationship between the microarray spacing and controllable droplet volume enabled the development of a programmable droplet manipulation platform with precision microfluidic and droplet screening capabilities. To demonstrate the versatility of PLG, the capture of different liquid droplets, including alkali solution (1 mol L^{-1} NaOH aqueous), acid solution (1 mol L^{-1} HCl aqueous), PBS buffer, cell culture medium (DMEM), blood, and high viscosity serum samples, is evaluated (Figure 2e, Video S4). Although the adhesion force of the serum sample (87 μN) is almost double that of the water droplet (43 μN) from the same PDMS layer, all the samples are successfully captured by the PLGs.

To precisely modulate the force state of the captured droplets and enable controlled release, the CLCP actuation layer within the PLG must exhibit remarkable and tunable photo-induced bending capabilities. Combined analysis via polarized optical microscopy (Figure S3) and 2D-WAXD (Figure S4) confirms the uniform alignment of the mesogens along the shearing direction within the nematic phase. Under UV irradiation (365 nm, 20 mW cm^{-2}), trans-cis photoisomerization of the azobenzene mesogens generates anisotropic contraction along the mesogen alignment axis, causing rapid macroscopic bending toward the light source (Figure 3a) [50]. The bending kinetics were found to be intensity-dependent: increasing the UV intensity from 10 to 30 mW cm^{-2} reduced the bending time from 8 to 4 s (Figure S6a). The 365 nm wavelength was selected because it corresponds to the maximum absorption peak of azobenzene, thereby maximizing the photoresponse efficiency [51]. Moreover, the intensity of 20 mW cm^{-2} represents a threshold below which the film bending becomes insufficient for actuation requirements (Figure S7). When exposed to visible light (530 nm, 30 mW cm^{-2}), the bent film recovers to the initial state with a consistent recovery performance of approximately 10 s (Figure S6b), as the asymmetric contraction disappears owing to the reversal of azobenzene from bent cis isomers to the trans state (Figure 3a). This combination of controllable bending speed and stable recovery performance substantiates the precise actuation capability of the CLCP layer. The bilayer PLG architecture combines this high-performance CLCP film (elastic modulus = 512 MPa) with the microarrayed PDMS substrate (~1 MPa), preserving the photoresponsive behavior observed in standalone CLCP films (Figure S5). Remarkably, the system maintains structural integrity through 100 cycles of alternating UV/Vis irradiation, with no interfacial delamination or degradation in terms of bending performance (Figure 3b, Video S5), demonstrating exceptional fatigue resistance attributable to the flexibility of the PDMS.

The droplet adhering to the surface of the PLG gradually ascends in spatial position during the bending process, thereby continuously accumulating gravitational potential energy. Owing to the variation in the curvature of the PLG, the droplet subsequently

TABLE 1 | Volume statistics of the transportable droplets of the bilayer devices.

Samples	V_{calmax} [a] [μL]	V_{expmax} [b] [μL]	V_{calmin} [c] [μL]	V_{expmin} [d] [μL]
D20	8.4	5.0	2.9	2.9
D30	4.0	4.0	1.5	1.5
D40	2.1	2.0	0.8	0.8
D50	1.1	1.0	0.5	0.5

[a] V_{calmax}: calculated maximum transportable droplet volume;
[b] V_{expmax}: experimental maximum transportable droplet volume;
[c] V_{calmin}: calculated minimum transportable droplet volume;
[d] V_{expmax}: experimental minimum transportable droplet volume.

slides along the surface and detaches from the PLG at a specific moment, completing the droplet release process (Figure 3c). Fluorescence imaging after droplets were mixed with a fluorescent reagent revealed no residual droplets on the PLG film after release, in contrast to the residual traces observed on pure PDMS under identical conditions (Figure S8), underscoring the superior nondestructive release performance of the PLG film. The gravity of an oversized droplet is larger than the adhesion provided by the PLG surface, while the gravitational potential-to-kinetic energy conversion of a small-volume droplet is insufficient to overcome its adhesion from the surface. A further quantitative analysis was performed to investigate the mechanism of droplet transport by these PLGs and evaluate their different liquid transport ranges. As shown in Figure 3d, the droplet is subjected to gravity G, adhesion of the microarray film F_{A1}, and adhesion of the substrate F_{A2} during the capture process. Therefore, the maximum volume of droplets that PLG can capture should satisfy the following equation:

$$F_{A1} - F_{A2} > G = \rho g V \tag{1}$$

where G is the gravitational potential energy of the droplet, ρ is the density of the liquid, g is the gravitational acceleration, and V is the volume of the liquid. The adhesion forces of the bilayer device (F_{A1}) and the substrate (F_{A2}) were taken into Equation (1), and the theoretical maximum volume V_{calmax} of the transportable droplets was calculated and is listed in Table 1. The experiments revealed that for D30, D40, and D50, the maximum droplet volume (V_{expmax}) that could be captured coincided with the calculated value. The only deviation is found from the maximum droplet size captured by PLG-D20 (5.0 μL), which is smaller than the calculated value (8.4 μL). This finding indicates that for larger droplets, their deformation is not negligible. This deformation leads to a larger contact area with the superhydrophobic substrate, which in turn results in greater adhesion.

During the droplet release process, the droplet is modeled as a sphere (Figure 3e) and is subjected to gravity G, surface friction f, and surface adhesion F_{A1}. When the gravity component along the tangential direction of the surface is greater than the friction component, the droplet begins to slide. This slide is controlled, resulting in a limited and predictable offset (as quantified in Table S1). Then, the gravitational potential energy of the droplet gradually transforms into the kinetic energy of the droplet, accelerating its rolling, so the centripetal force required to maintain its movement along the curved surface increases accordingly. When the adhesion is unable to provide sufficient centripetal force, the droplet slides off the arc. If the drop reaches the bottom of the arc (the position of the solid circle in Figure 3e) and is still stuck to the surface, it will not fall off. The centripetal force FC conforms to the following inequality:

$$F_{A1} - G > F_C = mv^2/r \tag{2}$$

where m and v represent the mass and velocity of the droplet, respectively. Notably, the adhesion force of PLG remains almost unchanged during the curvature change of PLG (Figure 3f), indicating that the adhesion force can be considered constant when the droplet rolls during the droplet release process caused by photo-induced deformation. Owing to their micrometer scale, the pillar tips on the PLG surface are significantly smaller than the curvature variation during bending, resulting in a negligible change in tip spacing. As confirmed in Figure S9, the measured variation in the microarray pitch before and after bending was less than 2%, which was considered insignificant.

In the bending process of the bilayer device, gravity was opposite to the frictional force when the liquid droplet was in the circle filled with the dotted line, and all of the gravity was used to counter the friction force. If the liquid droplet cannot slide down at this position, it cannot start to slide down at any position. Therefore, during the bending of the bilayer PLG, the maximum acceleration distance is from the circle filled with the dotted line in Figure 3e (the line connecting the center of the droplet and the center of the arc was horizontal) to the solid circle (the line connecting the center of the circle and the center of the arc was vertical). This characteristic ensures predictable droplet landing positions, thereby significantly enhancing the controllability of droplet release. The height (Δh) at which the drop fell is the radius of curvature of the arc (r). If the drop started to slide at this point, the speed obtained at the bottom of the arc would be the maximum, and the maximum kinetic energy value E_{kmax} was obtained according to the kinetic energy–potential energy conversion relationship:

$$E_{\text{kmax}} = mv^2/2 < mgr \tag{3}$$

According to Equations (2) and (3), the volume range of the transported droplets can be calculated:

$$V > F_{A1}/3\rho g \tag{4}$$

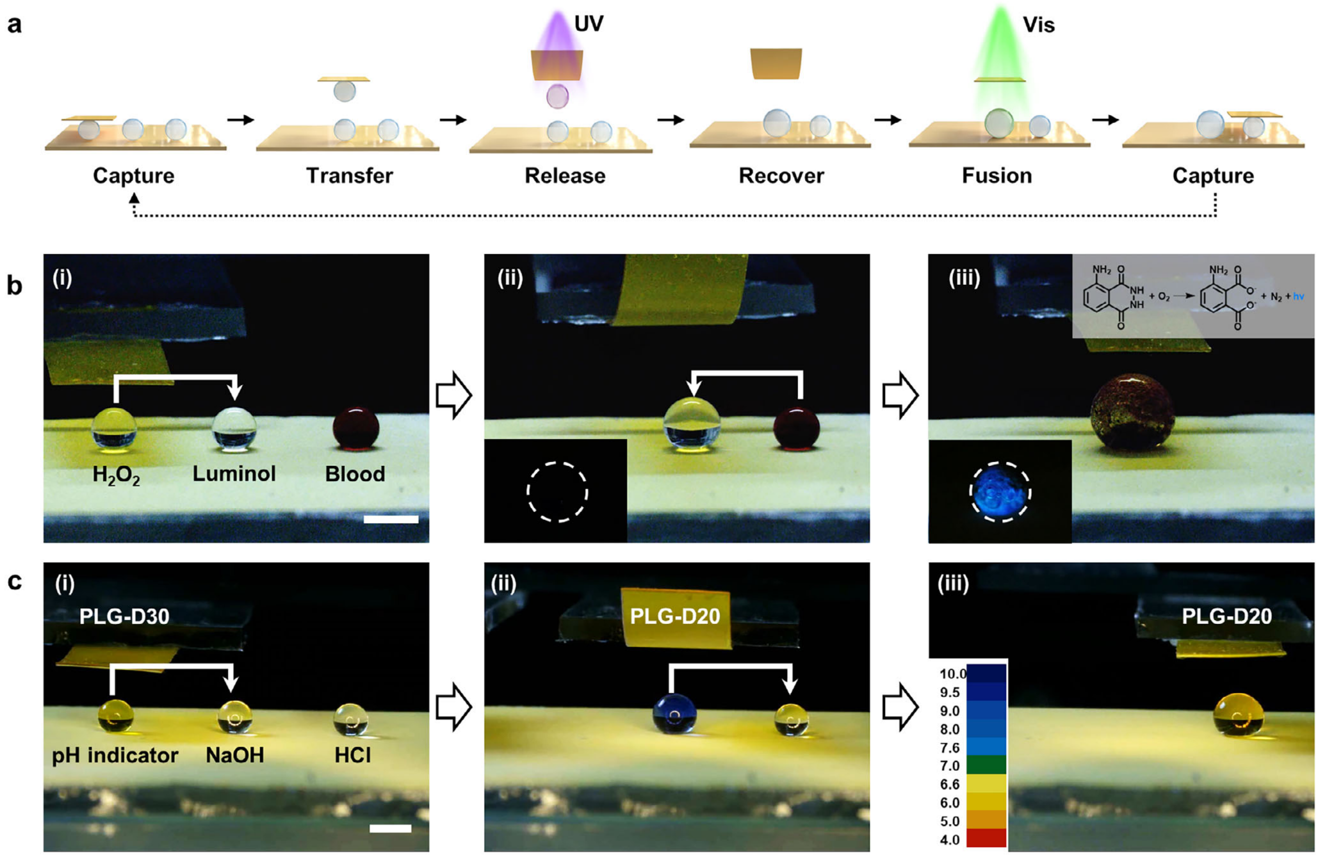

FIGURE 4 | (a) Schematic illustration showing the capture–release cyclic operation of PLG for droplet fusion and multistep chemical reactions. (b) The chemiluminescent luminol reaction for blood detection produces a distinctive blue glow when mixed with H_2O_2 and hemoglobin. The inserted pictures illustrate both the chemiluminescent phenomenon and the detailed chemical mechanism underlying the luminol reaction. The PLG in this case is D20. (c) Acid (HCl, 0.02 mol L^{-1}) and alkali (NaOH, 0.01 mol L^{-1}) neutralization reactions. The volume of drops is 2.5 μL. The PLG in this case is D30 and D20. The scale bar is 2 mm.

The adhesion of the bilayer device (F_{A1}) was taken into Equation (4) to calculate the minimum volume (V_{calmin}) of the transportable droplets, which is in good agreement with the experimental results from PLGs (Table 1). Moreover, to verify that the droplet of V_{calmin} can overcome the frictional force and slide along the curved surface, we tested the sliding angle (SA) of the droplets on the lower surface of the corresponding bilayer device, as shown in Table S2, which revealed that the droplets could slide off the surface. The transport of water droplets within a specific volume range can be achieved by adjusting the microarray spacing of the PLG. As illustrated in Figure S10, the PLG with a microarray spacing of 20–50 μm can precisely transport water droplets with a volume range of 0.5–5.0 μL.

Droplet fusion is accomplished via the capture–release cyclic operation of PLG, and the fused droplets can be further manipulated by employing PLG with a relatively high microarray density, which effectively facilitates the progression of multistep assays such as biomolecule detection (Figure 4a). As the most common sample matrix for biochemical assays, blood droplets with large amounts of proteins and cells are normally too viscous to be transported by conventional droplet manipulation methods that apply asymmetric surface-wetting gradients as the mechanism. In the context of mechanical pipettes, sample carryover residue in pipette tips results in cross-contamination and compromised volumetric precision [52]. Furthermore, the hydrodynamic shear stress generated during aspiration and dispensing may damage cellular integrity [53]. Taking advantage of nondestructive droplet transportation by PLG, we then investigated its potential in trace biomolecule detection. We employed the luminol reagent for the qualitative detection of blood to demonstrate 3D droplet transport (Figure 4b, Video S6). Three droplets (3.0 μL) of hydrogen peroxide, luminol, and blood were placed on the superhydrophobic surface. Owing to the good chemical resistance of PLG, the oxidative hydrogen peroxide droplet was successfully lifted and released upon UV irradiation (365 nm, 30 mW cm^{-2}) onto the luminol solution to form a fresh Diogene reagent. The PLG was then illuminated by visible light (530 nm, 30 mW cm^{-2}) to recover its flat state for the transport of the highly viscous blood sample. When the blood droplet was added to the mixture using a similar light-involved procedure, the iron ions in the red blood cells catalyzed the breakdown of hydrogen peroxide. This reaction generated singlet oxygen, which then oxidized luminol, producing the observed blue chemiluminescence. In another instance, a combination of two PLGs (PLG-D20 and PLG-D30 in this case) with different liquid transport ranges was applied to perform sequential pH analysis and reactions (Figure 4c, Video S7). A 2.5 μL aqueous droplet containing a pH indicator was first transported onto a NaOH aqueous droplet of the same size via PLG-D30. The color of the mixed droplet gradually changed

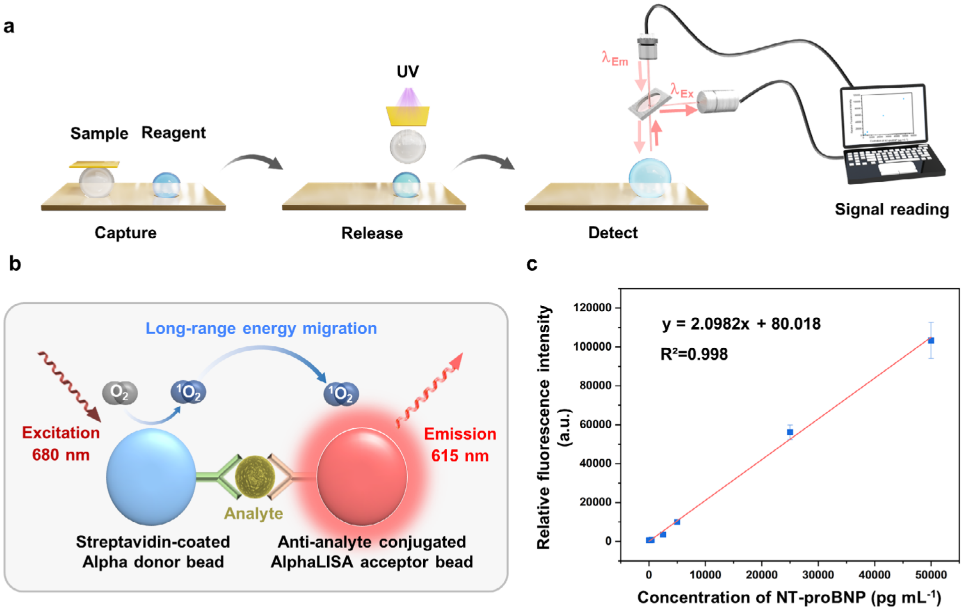

FIGURE 5 | (a) Schematic of the integrated platform, which employs a PLG for controlled droplet capture and transfer. (b) Diagram illustrating the signal transduction principle based on long-range energy migration between donor and acceptor labels within the formed immunocomplex. (c) Linear calibration curve showing the relationship between NT-proBNP concentration (pg mL^{-1}) and relative fluorescence intensity. Data are presented as mean ± SD from three independent measurements ($n = 3$). The straight line represents the linear regression equation ($y = 2.0982x + 80.018$, $R^2 > 0.99$).

from green to blue, indicating that the solution was alkaline. As the size of the mixed droplet was doubled, PLG-D30 was unable to lift it again, so it was replaced by PLG-D20 for the following reaction. Owing to the denser micropillars present on the surface, PLG-D20 produced enough adhesion force to lift the mixed droplet containing NaOH and the pH indicator while still being suitable for releasing the droplet with light. As a result, the mixed blue droplet fell off the PLG, reacting with the HCl droplet to produce an acidic droplet with an orange color. These demonstrations suggest that both chemical and high-viscosity samples can be manipulated by PLGs, expanding the applications of current droplet-based analysis.

To further demonstrate the nondestructive analytical capabilities of PLG, a bioassay platform was developed for droplet transfer and detection via PLG (Figure S11). This system was applied to an immunoassay for NT-proBNP (Figure 5a), a critical biomarker for diagnosing and stratifying heart failure risk [54]. Initially, 3.0 μL of the test sample and 1.0 μL of the NT-proBNP AlphaLISA immunoassay reagent were dispensed onto a low-adhesion surface. The sample droplet then adhered onto the PLG film and transported via a translation stage to a position above the reagent droplet. Upon UV light irradiation, the PLG releases the droplet, allowing it to fully merge and homogenously mix with the reagent. Subsequently, the PLG was employed to deliver the mixed droplet to the inlet of the detection unit. In the presence of NT-proBNP, streptavidin-coated donor beads functionalized with biotinylated anti-NT-proBNP antibodies and AlphaLISA acceptor beads conjugated with a second anti-NT-proBNP antibody were brought into proximity through antigen bridging. Under excitation at 680 nm, the donor beads generated singlet oxygen, which triggered a cascade chemiluminescence reaction in the acceptor beads, resulting in a characteristic emission peak at 615 nm (Figure 5b) [55]. This signal was captured via a highly sensitive fluorescence reader. Finally, the measured fluorescence intensity was converted into the concentration of NT-proBNP in the sample via computer processing. This prototype system delivers reliable and efficient detection performance owing to the precise droplet manipulation and nondestructive transport facilitated by the PLG film combined with the near-zero background interference characteristic of the AlphaLISA immunoassay. The system achieved accurate detection of NT-proBNP across a concentration range of 100 to 50 000 pg mL^{-1}, a performance comparable to that of commercial ELISA readers, thereby meeting clinical diagnostic requirements. Within the standard concentration range, the fitted calibration curve showed a high coefficient of determination ($R^2 = 0.998$, Figure 5c), further confirming the accuracy and nondestructive nature of droplet handling mediated by the PLG film. The precise control and nondestructive transport capabilities afforded by the PLG film underscore its strong potential for use in clinical diagnostics, environmental monitoring, food safety analysis, and broader biotechnology applications.

3 | Conclusions

In summary, we report the fabrication of a photocontrolled device featuring a novel transport strategy for 3D microdroplet manipulation. By combining a photodeformable CLCP with microarrayed PDMS, we achieve rapid capture and release of microdroplets via the conversion of gravitational potential energy to kinetic energy. Notably, 3D transport of diverse droplets including water, acid solutions, alkali solutions, cell culture media, and even blood is realized without altering surface adhesion, thereby overcoming limitations associated with conventional approaches. Moreover, by simply adjusting the microstructures of its surface, PLG allows the selective capture of droplets of particular sizes, providing a new tool for droplet screening. To further demonstrate the nondestructive performance of the PLG system, we applied it to a droplet-based immunoassay for NT-proBNP detection. The PLG-enabled precise transfer and merging of droplets yielded a standard curve with a high coefficient of determination ($R^2 = 0.998$), confirming its accuracy and potential in bioanalytical applications. We believe that this new transport mechanism may be adapted for other responsive systems for smart devices, and the further development of PLGs is promising for extending potential applications, such as cell screening and biodetection.

4 | Experimental Section

4.1 | Materials

The liquid crystal monomer DA11AB was synthesized according to the literature [45]. C6A was purchased from 800 Million Space-Time Liquid Crystal Technology Co., Ltd., and used after purification. The negative micropillar silicon wafer template was purchased from Beijing Blue Bird Yuanxin Microsystem Technology Co., Ltd. 1H, 1H, 2H, 2H-perfluorooctyl trichlorosilane was purchased from Sigma–Aldrich (97%).

4.2 | Preparation of the Superhydrophobic Low-adhesion Substrate

The fluorine-containing liquid crystal polymer was prepared according to the literature [49], dissolved in CH_2Cl_2 to prepare a 2 wt.% solution and filtered before electrospinning. The voltage used for electrospinning was 15 kV, and the receiver was aluminum foil. When electrospinning was completed, the sample on the aluminum foil was cut to a size of 20 mm × 30 mm and stuck on the surface of the glass sheet for future use.

4.3 | CLCP Films Preparation

First, a liquid crystal (LC) mixture containing monomers C6A, DA11AB, and photoinitiator Irgacure 784 at a molar ratio of 80: 20: 1 was injected into a 22 mm × 25 mm parallel-aligned LC cell at 102 °C (in an isotropic phase). The LC mixture was subsequently slowly cooled to 90°C (in the nematic phase) at a rate of 0.1 °C min^{-1} and polymerized under green light at 530 nm at 3 mW cm^{-2} for 2 h. After polymerization, the LC cell was opened, and the CLCP film was removed with a cutter.

4.4 | Preparation of the Microstructured PDMS Layer

First, the silicon wafer template with a negative microarray was modified with 1H, 1H, 2H, and 2H-perfluorooctyl trichlorosilane vapor at 100°C for 2 h. Then, the PDMS microarrayed film was prepared by vacuum casting the PDMS precursor (the mass ratio of monomer and cross-linking agent was 10:1) onto the modified template and cured in an oven at 80°C for 2 h. Finally, the microarrayed film was directly peeled off for use.

4.5 | Preparation of the CLCP/PDMS Bilayer Microarray Transfer Arm

The CLCP was directly pasted to the backside of the microarrayed PDMS to fabricate the bilayer film, which was then cut into a 10 mm × 5 mm rectangular shape with the LC orientation along the long axis. The bilayer film was stuck onto one end of a 15 mm × 30 mm glass sheet by silicone grease, and the other end of the glass sheet was adhered to the three-axis translation stage with double-sided adhesive to form the transfer arm.

4.6 | Characterization

The front and side morphology of PDMS microarray films, as well as the 45° angle topography of LCP/PDMS double-layer microarray films were observed by a field emission scanning electron microscope (FESEM, Zeiss, Ultra 55). The acceleration voltage used was 3 kV, and the samples were sprayed with gold before observation. The contact angle analysis of PDMS microarray surface, electrospun substrate surface, and the inverted roll angle of the surface of the PDMS microarray were conducted by an optical contact angle measuring instrument (Dataphysics, OCA20). The tensile stress-strain measurements of the LCP and PDMS microarray film were performed using an Instron Universal Testing Machine at a loading rate of 1 mm min^{-1}. Infrared thermographies were taken by the infrared thermal camera (FLIR, E64501). Photographs and videos of the morphology of PDMS microarray film as well as the light-induced droplet transport motions were taken by a super-resolution digital microscope (Keyence, VHX-1000C). Ultraviolet (UV, 365 nm) and visible (530 nm) light sources were produced from two LED irradiators (OMRON, ZUV-H30MC and CCS, HLV-24GR-3W), respectively. The surface adhesion force of PDMS microarray films with different pillar spacing, the adhesion of PDMS microarray films with different curvatures, and electrospun fluorine-containing liquid crystal polymer substrates were conducted by an adhesion tester (Dataphysics, DCAT25). The method is shown Figure S12: A 5 µL water droplet was suspended with a metal ring, and the superhydrophobic surface of sample that was approached and retracted from the suspended droplet at 0.005 mm s^{-1}. The force between the superhydrophobic surface and the water droplet was recorded during approach and retraction.

4.7 | Statistical Analysis

Where relevant, values are presented as the mean and corresponding standard deviation. The values of adhesion force and contact angle were obtained from three repeat measurements. The thickness of the CLCP and PDMS film, as well as the diameter and height of the microarrays, were measured from the TEM image of PLG using ImageJ software. For immunoassay NT-proBNP experiments, the calibration curve is fitted by the least squares method using Origin software. No data points were excluded as outliers. All statistical analyses were performed using Origin Pro.

Acknowledgements

This work was financially supported by the National Key R&D Program of China (2023YFC3605700), the National Natural Science Foundation of China (52233001), the Innovation Program of Shanghai Municipal Education Commission (2023ZKZD07), the Shanghai Rising-Star Program (22QA1401200), and the Foundation of the Shanghai Municipal Education Commission (24KXZNA05).

Conflicts of Interest

The authors declare no conflict of interest.

Data Availability Statement

The data that support the findings of this study are available from the corresponding author upon reasonable request.

References

1. D. J. Shin and T. H. Wang, "Magnetic Droplet Manipulation Platforms for Nucleic Acid Detection at the Point of Care," *Annals of Biomedical Engineering* 42 (2014): 2289–2302, https://doi.org/10.1007/s10439-014-1060-2.

2. H. Song, D. L. Chen, and R. F. Ismagilov, "Reactions in Droplets in Microfluidic Channels," *Angewandte Chemie International Edition* 45 (2006): 7336–7356, https://doi.org/10.1002/anie.200601554.

3. J. S. Barea, J. Lee, and D. K. Kang, "Recent Advances in Droplet-based Microfluidic Technologies for Biochemistry and Molecular Biology," *Micromachines* 10 (2019): 412, https://doi.org/10.3390/mi10060412.

4. F. Mei, H. Lin, L. Hu, W. Dou, H. Yang, and L. Xu, "Homogeneous, Heterogeneous, and Enzyme Catalysis in Microfluidics Droplets," *Smart Molecules* 1 (2023): 20220001, https://doi.org/10.1002/smo.20220001.

5. L. R. Shang, Y. Cheng, and Y. J. Zhao, "Emerging Droplet Microfluidics," *Chemical Reviews* 117 (2017): 7964–8040, https://doi.org/10.1021/acs.chemrev.6b00848.

6. Y. Zhang and N. T. Nguyen, "Magnetic digital microfluidics—a review," *Lab on a Chip* 17 (2017): 994–1008, https://doi.org/10.1039/c7lc00025a.

7. J. Lin, Y. Hou, Q. Zhang, and J. Lin, "Droplets in Open Microfluidics: Generation, Manipulation, and Application in Cell Analysis," *Lab on a Chip* 25 (2025): 787–805, https://doi.org/10.1039/d4lc00646a.

8. S. Sart, G. Ronteix, S. Jain, G. Amselem, and C. N. Baroud, "Cell Culture in Microfluidic Droplets," *Chemical Reviews* 122 (2022): 7061–7096, https://doi.org/10.1021/acs.chemrev.1c00666.

9. J. Yong, F. Chen, Q. Yang, J. Huo, and X. Hou, "Superoleophobic Surfaces," *Chemical Society Reviews* 46 (2017): 4168–4217, https://doi.org/10.1039/c6cs00751a.

10. P. Lv, Y. Zhang, D. Han, and H. Sun, "Directional Droplet Transport on Functional Surfaces with Superwettabilities," *Advanced Materials Interfaces* 8 (2021): 2100043, https://doi.org/10.1002/admi.202100043.

11. H. Wang, H. Lu, and W. J. Zhao, "A Review of Droplet Bouncing Behaviors on Superhydrophobic Surfaces: Theory, Methods, and Applications," *Physics of Fluids* 35 (2023): 021301, https://doi.org/10.1063/5.0136692.

12. L. Nan, H. Zhang, D. A. Weitz, and H. C. Shum, "Development and Future of Droplet Microfluidics," *Lab on a Chip* 24 (2024): 1135–1153, https://doi.org/10.1039/d3lc00729d.

13. H. Wang, Q. Zhang, X. Li, P. Yan, and Y. Guan, "High Precision Dynamic Manipulations of Large-Volume-Range Water-Based Droplets by a Soft Gripper with Robust Water-Repellent Superhydrophobic Surface," *Advanced Materials Technologies* 8 (2023): 2201599, https://doi.org/10.1002/admt.202201599.

14. H. Wang, S. Chen, H. Li, et al., "A Liquid Gripper Based on Phase Transitional Metallic Ferrofluid," *Advanced Functional Materials* 31 (2021): 2100274, https://doi.org/10.1002/adfm.202100274.

15. X. D. Wang, R. Zhang, Z. Q. Zhang, et al., "Three-dimensional Droplet Manipulation Using a PNIPAM-coated Mechanical Gripper," *Colloids and Surfaces a-Physicochemical and Engineering Aspects* 717 (2025), https://doi.org/10.1016/j.colsurfa.2025.136851.

16. C. Liu, X. Liu, and Q. Tang, et al., "3D Droplet Manipulation With Electrostatic Levitation," *Analytical Chemistry* 94 (2022): 8217–8225, https://doi.org/10.1021/acs.analchem.2c00178.

17. X. He, J. Zhang, B. Yang, X. Zhang, and Y. Deng, "Droplet Three-Dimension Manipulation in Parallel Liquid-infused Membrane Plates Configuration," *Sensors and Actuators B: Chemical* 330 (2021): 129344, https://doi.org/10.1016/j.snb.2020.129344.

18. K. Yang, S. Chen, Y. Liu, Y. Liang, Z. Zhang, and C. Liu, "Adhesion Switchable Transition on Bio-inspired Janus Surface for Multi-Directional Droplet Manipulation," *Chemical Engineering Journal* 496 (2024): 154254, https://doi.org/10.1016/j.cej.2024.154254.

19. X. Jing, H. Chen, L. Zhang, et al., "Accurate Magneto-Driven Multi-Dimensional Droplet Manipulation," *Advanced Functional Materials* 33 (2023): 2210883, https://doi.org/10.1002/adfm.202210883.

20. E. Zhang, Y. Wang, T. Lv, L. Li, Z. Cheng, and Y. Liu, "Bio-inspired Design of Hierarchical PDMS Microstructures with Tunable Adhesive Superhydrophobicity," *Nanoscale* 7 (2015): 6151–6158, https://doi.org/10.1039/c5nr00356c.

21. P. Brown, A. Bushmelev, C. P. Butts, et al., "Magnetic Control Over Liquid Surface Properties with Responsive Surfactants," *Angewandte Chemie International Edition* 51 (2012): 2414–2416, https://doi.org/10.1002/anie.201108010.

22. E. Guisasola, A. Baeza, and M. Talelli, et al.„ "Magnetic-Responsive Release Controlled by Hot Spot Effect," *Langmuir* 31 (2015): 12777–12782, https://doi.org/10.1021/acs.langmuir.5b03470.

23. D. L. Tian, N. Zhang, X. Zheng, et al., "Fast Responsive and Controllable Liquid Transport on a Magnetic Fluid/Nanoarray Composite Interface," *ACS Nano* 10 (2016): 6220–6226, https://doi.org/10.1021/acsnano.6b02318.

24. X. Liang, S. Guo, M. Chen, et al., "A Temperature and Electric Field-responsive Flexible Smart Film with Full Broadband Optical Modulation," *Materials Horizons* 4 (2017): 878–884, https://doi.org/10.1039/c7mh00224f.

25. Y. Takahashi, K. Fukuyasu, T. Horiuchi, Y. Kondo, and P. Stroeve, "Photoinduced Demulsification of Emulsions Using a Photoresponsive Gemini Surfactant," *Langmuir* 30 (2014): 41–47, https://doi.org/10.1021/la4034782.

26. K. Sumaru, K. Ohi, T. Takagi, et al., "Photoresponsive Properties of Poly(N-isopropylacrylamide) Hydrogel Partly Modified with Spirobenzopyran," *Langmuir* 22 (2006): 4353–4356, https://doi.org/10.1021/la052899.

27. L. Valli, G. Giancane, A. Mazzaglia, L. M. Scolaro, S. Conoci, and S. Sortino, "Photoresponsive Multilayer Films by Assembling Cationic Amphiphilic Cyclodextrins and Anionic Porphyrins at the Air/Water Interface," *Journal of Materials Chemistry* 17 (2007): 1660–1663, https://doi.org/10.1039/b703067c.

28. W. S. Yan, C. P. Zhao, W. Y. Luo, et al., "Optically Guided Pyroelectric Manipulation of Water Droplet on a Superhydrophobic Surface," *Acs Applied Materials and Interfaces* 13 (2021): 23181–23190, https://doi.org/10.1021/acsami.1c03407.

29. D. L. Herbertson, C. R. Evans, N. J. Shirtcliffe, G. McHale, and M. I. Newton, "Electrowetting on Superhydrophobic SU-8 Patterned Surfaces," *Sensors and Actuators A: Physical* 130 (2006): 189–193, https://doi.org/10.1016/j.sna.2005.12.018.

30. R. J. Vrancken, H. Kusumaatmaja, K. Hermans, et al., "Fully Reversible Transition From Wenzel to Cassie−Baxter States on

Corrugated Superhydrophobic Surfaces," *Langmuir* 26 (2009): 3335–3341, https://doi.org/10.1021/la903091s.

31. L. Sun, F. Bian, Y. Wang, Y. Wang, X. Zhang, and Y. Zhao, "Bioinspired Programmable Wettability Arrays for Droplets Manipulation," *Proceedings of the National Academy of Sciences* 117 (2020): 4527–4532, https://doi.org/10.1073/pnas.1921281117.

32. S. T. Wang, Y. L. Song, and L. Jiang, "Photoresponsive Surfaces with Controllable Wettability," *Journal of Photochemistry and Photobiology C: Photochemistry Reviews* 8 (2007): 18–29, https://doi.org/10.1016/j.jphotochemrev.2007.03.001.

33. D. Baigl, "Photo-actuation of Liquids for Light-driven Microfluidics: State of the Art and Perspectives," *Lab on a Chip* 12 (2012): 3637–3653, https://doi.org/10.1039/c2lc40596b.

34. M. Tenjimbayashi and K. Manabe, "A Review on Control of Droplet Motion Based on Wettability Modulation: Principles, Design Strategies, Recent Progress, and Applications," *Science and Technology of Advanced Materials* 23 (2022): 473–497, https://doi.org/10.1080/14686996.2022.2116293.

35. S. Jiang, Y. Hu, H. Wu, et al., "3D Multifunctional Magnetically Responsive Liquid Manipulator Fabricated by Femtosecond Laser Writing and Soft Transfer," *Nano Letters* 20 (2020): 7519–7529, https://doi.org/10.1021/acs.nanolett.0c02997.

36. X. Qing, L. Qin, W. Gu, and Y. Yu, "Deformation of cross-linked liquid crystal polymers by light—From ultraviolet to visible and infrared," *Liquid Crystals* 43 (2016): 2114–2135, https://doi.org/10.1080/02678292.2016.1217358.

37. J. Wei and Y. Yu, "Photodeformable Polymer Gels and Crosslinked Liquid-crystalline Polymers," *Soft Matter* 8 (2012): 8050–8059, https://doi.org/10.1039/c2sm25474c.

38. G. Cheng, C. Y. Kuan, K. W. Lou, and Y. Ho, "Light-Responsive Materials in Droplet Manipulation for Biochemical Applications," *Advanced Materials* 37 (2025): 2313935, https://doi.org/10.1002/adma.202313935.

39. Y. Liu, J. Ma, Y. Yang, et al., "Smart Chiral Liquid Crystal Elastomers: Design, Properties and Application," *Smart Molecules* 2 (2024): 20230025, https://doi.org/10.1002/smo.20230025.

40. L. Jiang, L. Qin, F. Pan, and Y. Yu, "All-Optical Microfluidic Technology Enabled by Photodeformable Linear Liquid Crystal Polymers," *Accounts of Materials Research* 6 (2025): 274–284, https://doi.org/10.1021/accountsmr.4c00318.

41. J. Lv, Y. Liu, J. Wei, E. Chen, L. Qin, and Y. Yu, "Photocontrol of Fluid Slugs in Liquid Crystal Polymer Microactuators," *Nature* 537 (2016): 179–184, https://doi.org/10.1038/nature19344.

42. K. M. Herbert, H. E. Fowler, J. M. McCracken, K. R. Schlafmann, J. A. Koch, and T. J. White, "Synthesis and Alignment of Liquid Crystalline Elastomers," *Nature Reviews Materials* 7 (2022): 23–38, https://doi.org/10.1038/s41578-021-00359-z.

43. X. Qing, J. Lv, and Y. Yu, "Photodeformable Liquid Crystal Polymers," *Acta Polymerica Sinica* (2017): 1679–1705, https://doi.org/10.11777/j.issn1000-3304.2017.17196.

44. Y. Pu, X. Zhang, X. Liu, X. Zhao, Z. Yang, and Y. Yu, "Multistimuli Responsive Bionic Actuators Constructed by Linear Liquid Crystal Polymers," *Transactions of Materials Research* 1 (2025): 100003, https://doi.org/10.1016/j.tramat.2025.100003.

45. Y. Zhang, J. Xu, F. Cheng, R. Yin, C. Yen, and Y. Yu, "Photoinduced Bending Behavior of Crosslinked Liquid-crystalline Polymer Films with a Long Spacer," *Journal of Materials Chemistry* 20 (2010): 7123–7130, https://doi.org/10.1039/c0jm00510j.

46. Y. Z. Wang, H. Lai, Z. J. Cheng, et al., "Smart Superhydrophobic Shape Memory Adhesive Surface Toward Selective Capture/Release of Microdroplets," *Acs Applied Materials & Interfaces* 11 (2019): 10988–10997, https://doi.org/10.1021/acsami.9b00278.

47. D. E. Packham, "Surface energy, surface topography and adhesion," *International Journal of Adhesion and Adhesives* 23 (2003): 437–448, https://doi.org/10.1016/s0143-7496(03)00068-x.

48. Z. Lian, J. Zhou, W. Ren, et al., "Recent Progress in Bio-inspired Macrostructure Array Materials with Special Wettability—from Surface Engineering to Functional Applications," *International Journal of Extreme Manufacturing* 6 (2024): 012008, https://doi.org/10.1088/2631-7990/ad0471.

49. X. Zhang, L. Qin, Y. Liu, J. Wei, and Y. Yu, "Manipulating Small Water Droplets on a Photo-switchable Mat of Fluorinated Linear Liquid Crystal Polymers," *Giant* 2 (2020): 100019, https://doi.org/10.1016/j.giant.2020.100019.

50. X. Pang, J. Lv, C. Zhu, L. Qin, and Y. Yu, "Photodeformable Azobenzene-Containing Liquid Crystal Polymers and Soft Actuators," *Advanced Materials* 31 (2019): 1904224, https://doi.org/10.1002/adma.201904224.

51. B. Ranjitha, D. Sandhya Kumari, A. Shetty, et al., "Impact of Terminal Group on Azobenzene Liquid Crystal Dimers for Photo-Responsive Optical Storage Devices," *Journal of Molecular Liquids* 383 (2023): 121985, https://doi.org/10.1016/j.molliq.2023.121985.

52. A. Shakeri, H. Yousefi, N. A. Jarad, et al., "Contamination and Carryover Free Handling of Complex Fluids using Lubricant-infused Pipette Tips," *Scientific Reports* 12 (2022), https://doi.org/10.1038/s41598-022-18756-x.

53. Y. Xie, F. Wang, E. Puscheck, and D. Rappolee, "Pipetting Causes Shear Stress and Elevation of Phosphorylated Stress-activated Protein Kinase/jun Kinase in Preimplantation Embryos," *Molecular Reproduction and Development* 74 (2007): 1287–1294, https://doi.org/10.1002/mrd.20563.

54. M. Adamo, M. Pagnesi, A. Mebazaa, et al., "NT-proBNP and High Intensity Care for Acute Heart Failure: The STRONG-HF trial," *European Heart Journal* 44 (2023): 2947–2962, https://doi.org/10.1093/eurheartj/ehad335.

55. M. Bielefeld-Sevigny, "AlphaLISA Immunoassay Platform—The "No-Wash" High-Throughput Alternative to ELISA," *ASSAY and Drug Development Technologies* 7 (2009): 90–92, https://doi.org/10.1089/adt.2009.9996.

Supporting Information

Additional supporting information can be found online in the Supporting Information section.

Supporting File 1: smtd70588-sup-0001-SuppMat.docx.
Supporting File 2: smtd70588-sup-0002-VideoS1.avi.
Supporting File 3: smtd70588-sup-0003-VideoS2.avi.
Supporting File 4: smtd70588-sup-0004-VideoS3.avi.
Supporting File 5: smtd70588-sup-0005-VideoS4.avi.
Supporting File 6: smtd70588-sup-0006-VideoS5.avi.
Supporting File 7: smtd70588-sup-0007-VideoS6.avi.
Supporting File 8: smtd70588-sup-0008-VideoS7.avi.